coatings

MDPI

Article

$Na_2SO_4 + V_2O_5$ Corrosion Behavior of $BaNd_2Ti_3O_{10}$ for Thermal Barrier Coating Applications

Yajuan She, Yiwen Guo, Zanxian Tan and Kai Liao *

School of Mechanical and Electrical Engineering, Hunan Applied Technology University, Changde 415000, China; sheyajuan94@163.com (Y.S.); yiwen123qwe@163.com (Y.G.); Tzx888UT@163.com (Z.T.)

* Correspondence: liaokai102@csuft.edu.cn

Received: 15 August 2020; Accepted: 16 September 2020; Published: 20 September 2020

Abstract: $BaNd_2Ti_3O_{10}$ has been considered as a promising thermal barrier coating (TBC) candidate material, which reveals many advantages over the widely used TBC material of yttria partially stabilized zirconia, such as lower thermal conductivity, better high-temperature capability, and higher resistance to environmental deposits corrosion. In this study, the hot corrosion behavior of $BaNd_2Ti_3O_{10}$ in $Na_2SO_4 + V_2O_5$ molten salt at 900 °C and 1000 °C is investigated. Exposed to the salt for 4 h at 900 °C, $BaNd_2Ti_3O_{10}$ pellets had an obvious reaction with the salt, forming corrosion products of $NdVO_4$, TiO_2, and $BaSO_4$, and the reaction layer was ~30 μm, beneath which no salt trace could be found. Prolonging the corrosion time to 20 h, the type of the corrosion products had no change. At an elevated corrosion temperature of 1000 °C for 4 h, the corrosion products were still $NdVO_4$, TiO_2, and $BaSO_4$, but $NdVO_4$ revealed a significant growth, which fully covered the pellet surface. The mechanisms by which the corrosion reaction between $BaNd_2Ti_3O_{10}$ and the molten salt occurred were discussed.

Keywords: thermal barrier coating; $BaNd_2Ti_3O_{10}$; hot corrosion; $Na_2SO_4 + V_2O_5$; Corrosion mechanism

1. Introduction

Thermal barrier coatings (TBCs) are extensively used onto the hot-components (blades, vanes, and combustion chamber) of turbine engines, which give rise to thermal insulation and protect metallic parts from corrosion, increasing the efficiency and performance of turbines [1–3]. A typical TBC system usually consists of a ceramic topcoat and a bond coat, the latter of which is designed to enhance the oxidation and corrosion resistance, as well as to improve the adhesion between the ceramic top coat and the substrate. The ceramic top coat is commonly made of yttria partially stabilized zirconia (YSZ), and is usually fabricated by air plasma spraying (APS) and electron beam physical vapor deposition (EB-PVD) [4–6]. YSZ TBCs have revealed many advantages, such as low thermal conductivity, excellent toughness, and good thermal expansion match with the substrate [1,7–9].

In marine environments or for the usage of low-quality fuel, TBCs face problems of molten salt attack, which caused by vanadium, sulfur, and phosphorous from fuel impurities or corrosive environments condensing the coating surfaces [10–15]. At 600–1000 °C, molten salt corrosion to YSZ TBCs is rather severe. The salt melts at high temperatures and infiltrates into the coating, during which a reaction between molten salt and YSZ occurs, decreasing the stabilizer in the TBC. As a result, the coating would undergo an undesirable phase transformation, causing failure much more quickly than if no molten salt is present [16–19]. Although the degradation mechanism by which molten salt attacks YSZ TBCs has been clear, measurements to solve the corrosion issue still need large studies, and some researchers have made some attempts [15,20–25], such as introducing Al_2O_3, CeO_2, Ta_2O_5, and RE_2O_3 (RE = rare earth) into the ZrO_2-based system as a new stabilizer or co-dopants.

In order to further improve engine efficiency, there are great motivations for increasing the engine-operating temperature. However, YSZ TBCs have an operation temperature limitation (1200 °C), above which they suffer from phase transformation and thermal conductivity increasing. Moreover, a practical requirement for TBCs is that the thermal conductivity should be as low as possible for better thermal insulation. Therefore, alternative TBC materials are largely required with even better phase stability, improved thermo-physical and mechanical properties, and superior high-temperature capability. However, for these novel TBCs operated at higher temperatures, threats resulting from molten salts still exist. Hence, it is necessary to understand the hot corrosion behavior of newly developed TBC materials in molten salts.

Recently, the hot corrosion behavior of some TBC candidate materials exposed to molten salt has been evaluated. Ouyang et al. reported the hot corrosion behavior of $Gd_2Zr_2O_7$ and $Yb_2Zr_2O_7$ ceramics in V_2O_5 molten salt, and investigated the associated mechanisms [13,26]. Guo et al. indicated that $(Sm_{0.5}Sc_{0.5})_2Zr_2O_7$ has a better corrosion resistance to Na_2SO_4 + V_2O_5 molten salt than $Sm_2Zr_2O_7$ [27]. Cao et al. studied the corrosion products of $LaTi_2Al_9O_{19}$ ceramic resulting from V_2O_5 salt attack, and discussed their formation mechanisms [14]. Chen et al. investigated the corrosion behavior of plasma sprayed $LaMg_2Al_9O_{19}$ coatings in V_2O_5 molten salt [28]. $BaNd_2Ti_3O_{10}$ belongs to $BaLn_2Ti_3O_{10}$ (Ln: La, Nd, Sm) series, which is a perovskite derivative. It has been reported that $BaLn_2Ti_3O_{10}$ has low thermal conductivities, good high-temperature capability, and excellent resistance to environmental deposits corrosion, giving rise to be promising TBC candidate materials [29,30]. Additionally, $BaLn_2Ti_3O_{10}$ TBCs have been successfully produced by Guo et al., which have better thermal cycling performance than YSZ TBCs [31]. However, how $BaNd_2Ti_3O_{10}$ performs in molten salt is still unclear, and no report on the hot corrosion behavior of $BaNd_2Ti_3O_{10}$ exposed to molten salt exists in open literature.

In this study, the Na_2SO_4 + V_2O_5 corrosion behavior of $BaNd_2Ti_3O_{10}$ for possible use as a novel TBC material is investigated at 900 °C for 4 h and 20 h, and 1000 °C for 4 h. The emphasis is analyzing the corrosion products of $BaNd_2Ti_3O_{10}$ due to molten salt exposure by using dense pellets, based on which the related corrosion mechanisms are discussed.

2. Experimental Procedure

$BaCO_3$, TiO_2, and Nd_2O_3 powders are used as raw materials to produce $BaNd_2Ti_3O_{10}$ powder by a solid-state reaction method. The raw materials mixed with an appropriate quantity were ball milled in ionized water at a speed of 400 rpm for 10 h, following by drying at 160 °C for 10 h and calcination at 1500 °C for 24 h. The process was repeated until pure $BaNd_2Ti_3O_{10}$ powder was fabricated. $BaNd_2Ti_3O_{10}$ pellets for hot corrosion tests were prepared by cold pressing at ~250 MPa, followed by sintering at 1500 °C for 10 h.

Hot corrosion tests were conducted using Na_2SO_4 + V_2O_5 salt (50 mol% Na_2SO_4 and 50 mol% V_2O_5) in a furnace. Prior to the tests, pellets were grinded by 800# SiC papers, followed by ultrasonic cleaning in ethanol and drying at 120 °C. Na_2SO_4 + V_2O_5 salt was uniformly spread on the pellet surface by using a very fine glass rod. The salt content on the pellet surface was ~10 mg/cm^2, which was determined by calculating the weight difference between the samples before and after the salt coverage. $BaNd_2Ti_3O_{10}$ pellets covered with Na_2SO_4 + V_2O_5 salt were isothermally heated in a furnace, followed by cooling down to room temperature with the furnace. The heat treatment conditions were as follows: 900 °C for 4 h and 20 h, and 1000 °C for 4 h.

X-ray diffraction (XRD; Rigaku Diffractometer, CuKa radiation, Tokyo, Japan) was employed to conduct phase composition analysis, and the scanning angle (2θ) range was 10°–80° with a scanning rate of 0.1°/s. The peak identification was carried out using MDI Jade 6.0 software. Surface morphologies and composition analysis were conducted by a scanning electron microscope (SEM; TDCLS4800, Hitachi Ltd., Tokyo, Japan) equipped with energy dispersive spectroscopy (EDS, IE 350), and cross-sectional microstructure was analyzed using a scanning electron microscope (SEM; TDCLSU1510, Hitachi Ltd.,

Japan). For cross-section observations, the samples were cold mounted in epoxy resin, and then grinded by 150#, 400#, 800#, 1200#, and 2000# SiC papers, following by polishing with diamond pastes (5 μm size).

3. Results and Discussion

Figure 1a shows the surface microstructure of $BaNd_2Ti_3O_{10}$ bulk. It has inhomogeneous grains, with an average size of 5–10 μm. The cross-sectional microstructure is shown in Figure 1b. The fabricated pellet reveals a dense microstructure, and few pores could be found, the relative density of which is above 95%. According to the surface and cross-section observations, it could be considered that in the following corrosion experiments, the salt penetration might be limited due to the dense microstructure of the pellet, and the corrosion may occur at the surface regions resulting from the reaction between molten salt and $BaNd_2Ti_3O_{10}$.

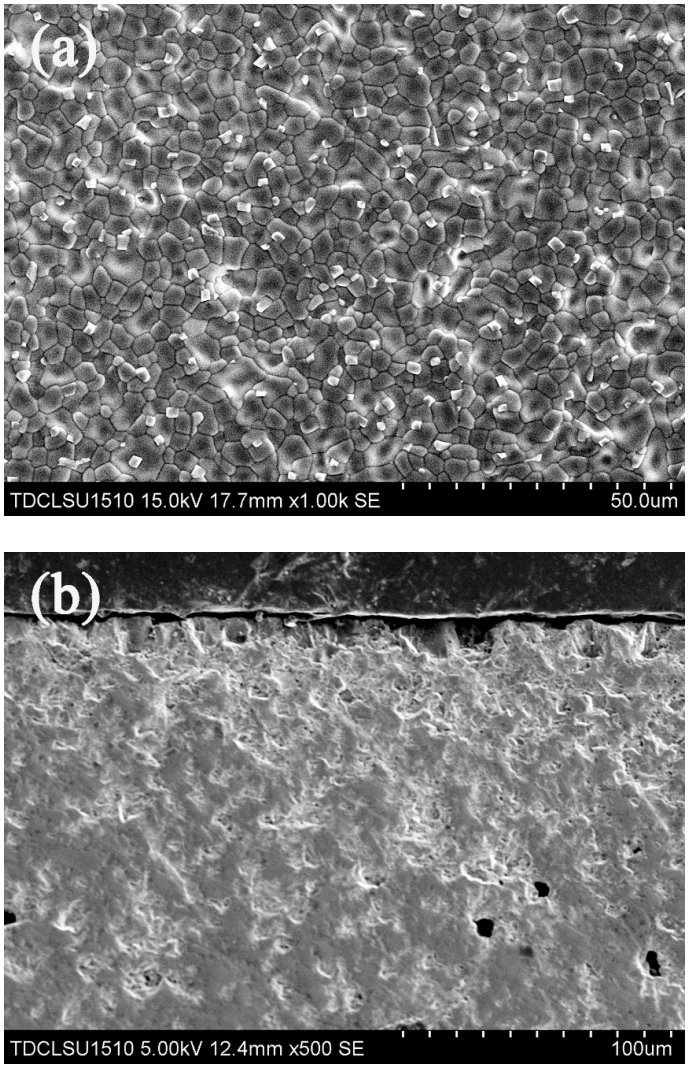

Figure 1. Surface (**a**) and cross-section (**b**) microstructures of $BaNd_2Ti_3O_{10}$ pellet.

Figure 2 shows the XRD patterns of $BaNd_2Ti_3O_{10}$ pellets after hot corrosion tests in Na_2SO_4 + V_2O_5 salt, and that of the as-fabricated pellet is also presented for comparison. Exposed to 900 °C for 4 h and 20 h, the sample surfaces have similar XRD patterns, consisting of diffraction peaks ascribed to $NdVO_4$, TiO_2, and $BaSO_4$. This suggests that the corrosion leads to the formation of these products, the types of which are corrosion time independent at 900 °C. Additionally, the substrate phase ($BaNd_2Ti_3O_{10}$) is detected, which indicates that the corrosion on the surface is uneven causing

some regions are uncorroded, or the reaction layer on the surface is thin. After corrosion at 1000 °C for 4 h, only $NdVO_4$ and some TiO_2 could be detected by XRD, which might be because that the corrosion product of $NdVO_4$ largely grows covering the pellet surface. This will be further confirmed by SEM observations in the following sections.

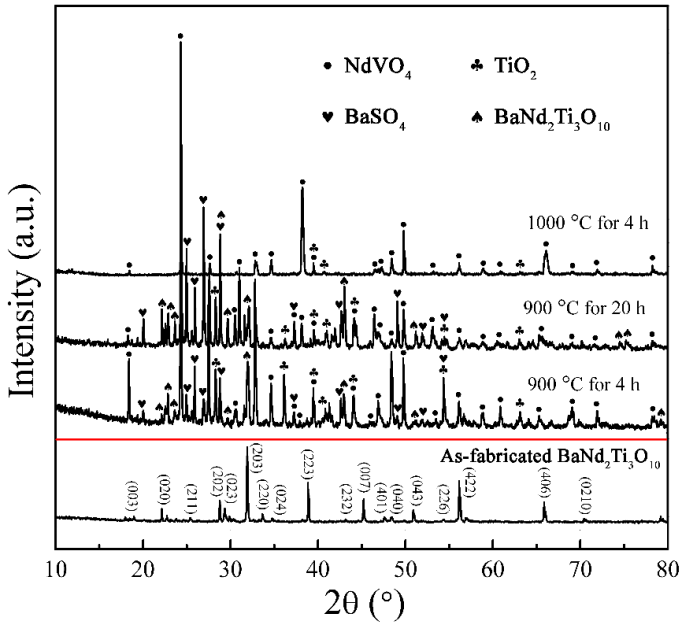

Figure 2. XRD patterns of the as-fabricated $BaNd_2Ti_3O_{10}$ pellet and the pellets after hot corrosion in Na_2SO_4 + V_2O_5 salt at 900 °C for 4 h and 20 h, and 1000 °C for 4 h.

Figure 3 shows typical surface morphologies of $BaNd_2Ti_3O_{10}$ sample after hot corrosion at 900 °C for 4 h. It is evident that many corrosion products are formed on the sample surface, as shown in Figure 3a. In Figure 3b showing these products at a higher magnification, it could be found that they have three different shapes, i.e., rod shaped (marked as A) particle shaped (marked as B), and plate shaped (marked as C), and their chemical compositions are listed in Table 1. Compound A consists of Nd, V, and O, compound B has Ti and O, while compound C is composed of Ba, S, and O. Based on the above XRD results, one could determine that compounds A, B, and C are $NdVO_4$, TiO_2, and $BaSO_4$, respectively.

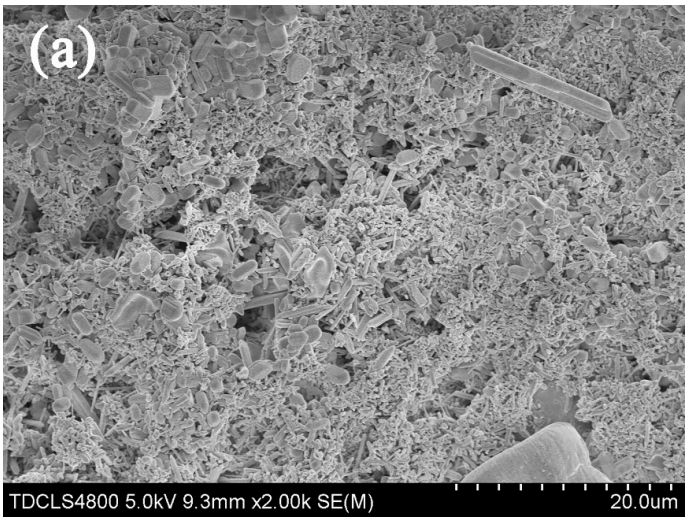

Figure 3. *Cont.*

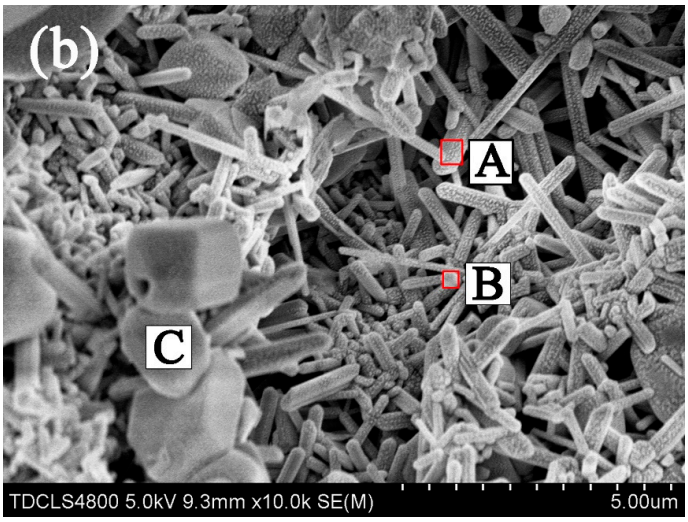

Figure 3. Surface morphologies of $BaNd_2Ti_3O_{10}$ pellet after hot corrosion in Na_2SO_4 + V_2O_5 molten salt at 900 °C for 4 h. (**a**) and (**b**) show the images with different magnifications.

Table 1. Chemical compositions of compounds A–C in Figure 3 (in at.%).

Compound	Ba	Nd	Ti	V	S	O
A	-	17.1	-	18.3	-	64.6
B	-	-	33.4	-	-	66.6
C	16.8	-	-	-	17.8	65.4

The cross-sectional microstructure of the sample after corrosion at 900 °C for 4 h is shown in Figure 4a. A significantly different layer with a thickness of ~30 μm can be observed on the sample surface, in which some parts are dense and other regions are rather loose. Beneath this reaction layer, the pellet keeps structure integrity, and has no molten salt trace. In an enlarged image as shown in Figure 4b, the dense parts could be identified as the original substrate, which could provide the explanation for the detection of $BaNd_2Ti_3O_{10}$ phase by XRD, and the loose regions are composed of corrosion products, which are composed of rod shaped $NdVO_4$ and particle shaped TiO_2. One could find that, at the interface of the reaction layer and the original substrate, there are some pores, which might be attributed to the thermal expansion mismatch between the newly formed layer and the original $BaNd_2Ti_3O_{10}$ pellet.

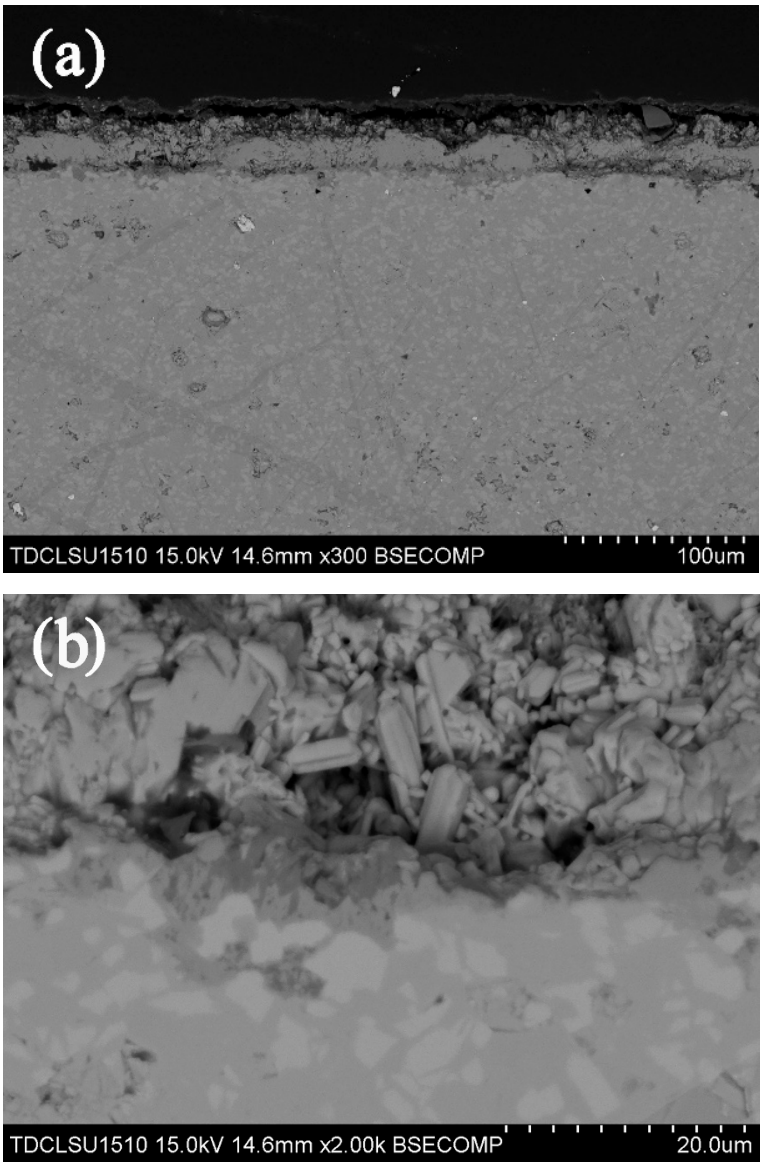

Figure 4. Cross-sectional microstructures of $BaNd_2Ti_3O_{10}$ pellet after Na_2SO_4 + V_2O_5 molten salt corrosion at 900 °C for 4 h. (**a**) and (**b**) show the images with different magnifications.

Figure 5 shows the SEM images of the $BaNd_2Ti_3O_{10}$ sample exposed to corrosion at 900 °C for 20 h. This is similar to the case of 4 h corrosion; corrosion products are also evident in this case, as shown in Figure 5a. Enlarging this image, one could clearly observe these differently shaped corrosion products, i.e., rod shaped (D), particle shaped (E) and plate shaped (F), as presented in Figure 5b. EDS was employed to analyze the chemical composition of these products, and the results are also listed in Table 2. Compound D contains Nd, V, and O, compound E is composed of Ti and O, while crystal F consists of Ba, S, and O. According to the above XRD results, it could be confirmed that D, E, and F are $NdVO_4$, TiO_2, and $BaSO_4$, respectively.

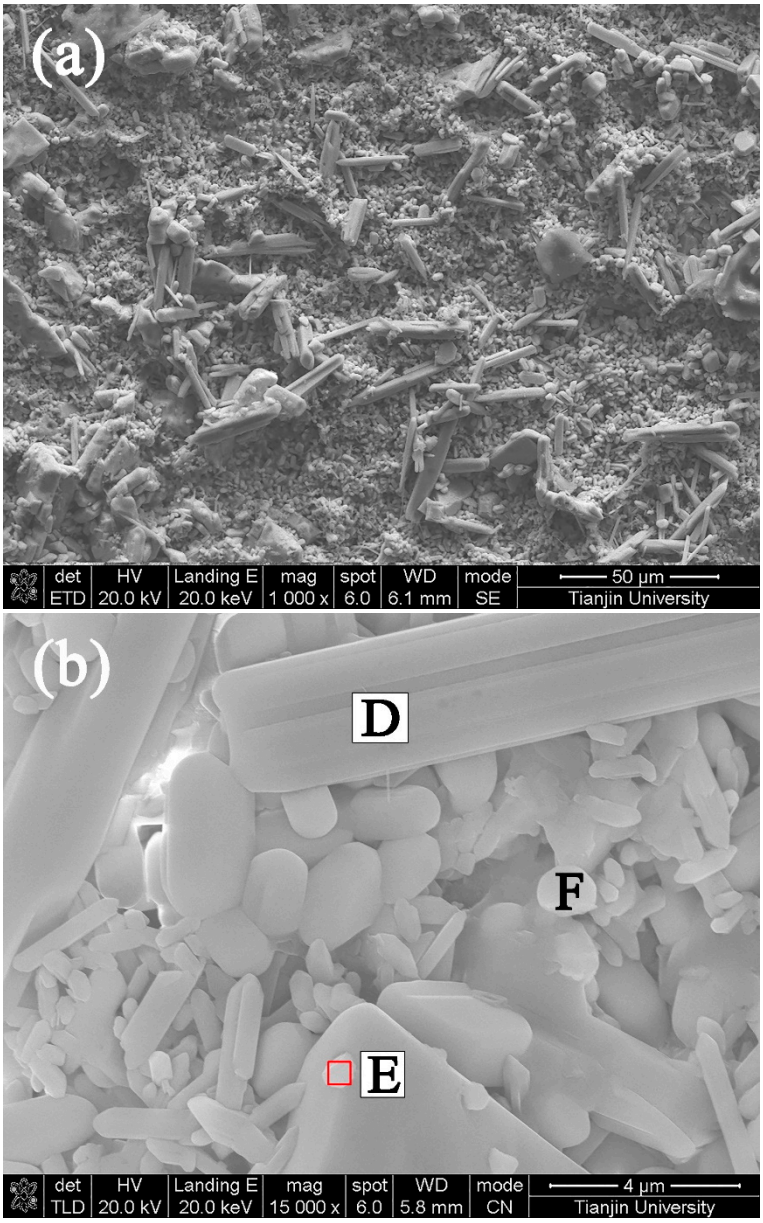

Figure 5. Surface morphologies of $BaNd_2Ti_3O_{10}$ pellet after Na_2SO_4 + V_2O_5 molten salt corrosion at 900 °C for 20 h. (**a**) and (**b**) show the images with different magnifications.

Table 2. Chemical compositions of compounds D–F in Figure 5 (in at.%).

Compound	Ba	Nd	Ti	V	S	O
D	-	18.5	-	19.3	-	62.2
E	-	-	32.9	-	-	67.1
F	17.1	-	-	-	18.9	64.0

$BaNd_2Ti_3O_{10}$ sample was subjected to hot corrosion in Na_2SO_4 + V_2O_5 salt at 1000 °C for 4 h, and its surface morphologies are shown in Figure 6. The sample surface is almost completely covered by corrosion products, as shown Figure 6a. In the enlarged image (Figure 6b), the corrosion product with a rod shape could be clearly observed, but other shaped products are rare, only presenting a few particle shaped compounds. EDS analysis of the rod-shaped compound indicates that it is composed of Nd, V, and O, and could be identified as $NdVO_4$ in combination with the XRD result. The particle shaped corrosion products are TiO_2 based on EDS and XRD analysis. $BaSO_4$ and $BaNd_2Ti_3O_{10}$ are

not detected by SEM, mainly attributed to the significant growth of $NdVO_4$ which covers the whole surface of the sample.

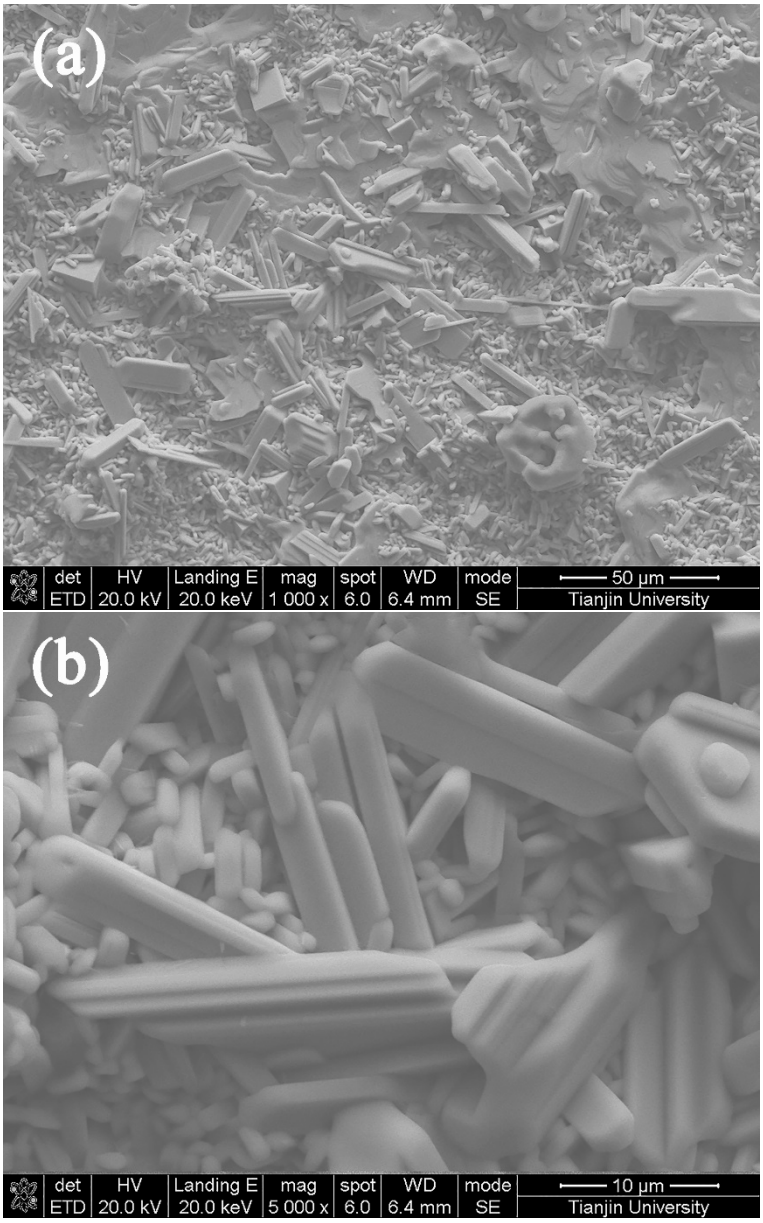

Figure 6. Surface morphologies of $BaNd_2Ti_3O_{10}$ pellet after Na_2SO_4 + V_2O_5 molten salt corrosion at 1000 °C for 4 h. (**a**) and (**b**) show the images with different magnifications.

Based on the aforementioned observations, it could find that in the presence of Na_2SO_4 + V_2O_5 molten salt, $BaNd_2Ti_3O_{10}$ undergoes evident corrosion, and the type of corrosion products are temperature and time independent, which consists of $NdVO_4$, TiO_2, and $BaSO_4$. However, an elevated temperature causes significant growth of $NdVO_4$, which can cover the whole surface of the sample. The mechanism for the formation of these corrosion products could be understood in terms of the breakdown of the chemical bonds of $BaNd_2Ti_3O_{10}$ by molten salt [14,32]. From the viewpoint of crystallography, $BaNd_2Ti_3O_{10}$ crystal has a lattice consisting of a tri-perovskite [$Nd_2Ti_3O_{10}$] layer separated by a Ba layer along c-axis [29,30]. In the lattice, the Ba insertion layers are weakly bonded, which are easy to be destroyed by molten salt. As a result, Ba-O bonds in $BaNd_2Ti_3O_{10}$ lattice is expected to first break due to molten salt attack, giving rise to the formation of Ba contained corrosion

products. Then, Nd and Ti are enriched in the crystal due to the consumption of Ba, which provides a greater chance for the salt to destroy Nd-O and Ti-O bonds. Thus, other corrosion products containing Nd and Ti are expected to be generated.

For the mixture of Na_2SO_4 and V_2O_5 salts, a reaction occurs above 900 °C by the following expression [11,18,27,33]:

$$Na_2SO_4(l) + V_2O_5(l) \rightarrow 2NaVO_3(l) + SO_3(g) \quad (1)$$

In this study, the formed products resulting from Equation (1) react with $BaNd_2Ti_3O_{10}$ pellets. Based on the reaction products analysis by XRD and SEM, the reaction between $BaNd_2Ti_3O_{10}$ and the molten salt could be expressed by the following equation:

$$BaNd2Ti3O10(s) + 2NaVO3(l) + SO3(g) \rightarrow BaSO4(s) + 2NdVO4(s) + 3TiO2(s) + Na2O(s) \quad (2)$$

It has been reported that for YSZ pellets or coatings, molten salt has a large tendency to penetrate inside, reacting with YSZ to form YVO_4 and m-ZrO_2, which causes a large and deep reaction region, where the phase composition and microstructure are largely destroyed [17–19,21]. By comparison, in the presence of Na_2SO_4 + V_2O_5 molten salt, there is only a ~30 μm thickness destroyed region/layer on the $BaNd_2Ti_3O_{10}$ pellet surface, beneath which no molten salt trace could be found (Figure 4). Although EDS line scans or maps of this layer is not provided here, based on the identified reaction products on the pellet surface and cross-section observations, one could confirm that the destroyed region is composed of reaction products. The formation of these corrosion products has largely consumed the salt; as a result, very limited molten salt can infiltrate the deep regions of the pellets. In other words, the reaction layer could be considered as a sacrificial layer, the formation of which can protect the pellet or coating from severe damage. Hence, $BaNd_2Ti_3O_{10}$ is resistant to Na_2SO_4 + V_2O_5 salt corrosion to a certain extent; especially, its resistance to molten salt corrosion is better than YSZ.

4. Conclusions

$BaNd_2Ti_3O_{10}$, a promising TBC candidate material, was exposed to Na_2SO_4 + V_2O_5 molten salt at 900 °C and 1000 °C to evaluate its hot corrosion resistance. After exposure to Na_2SO_4 + V_2O_5 salt for 4 h at 900 °C, there was an obvious reaction between $BaNd_2Ti_3O_{10}$ and the salt, producing $NdVO_4$, TiO_2, and $BaSO_4$ as the corrosion products, which formed a reaction layer with a thickness of ~30 μm, and the regions beneath the reaction layer were not destroyed by the molten salt. At 900 °C for 20 h in the salt, the type of corrosion products of $BaNd_2Ti_3O_{10}$ pellet had no change. At an elevated corrosion temperature of 1000 °C for 4 h, although the corrosion products were still $NdVO_4$, TiO_2, and $BaSO_4$, $NdVO_4$ crystals grew significantly and fully covered the pellet surface. Based on the research results, $BaNd_2Ti_3O_{10}$ is found to have a good resistance to Na_2SO_4 + V_2O_5 salt corrosion, and due to the excellent high-temperature capability and thermo-physical properties, it has a potential application for TBCs, especially under the corrosive environments containing vanadium and sulfur.

Author Contributions: Conceptualization, Y.S. and K.L.; methodology, Y.S. and Y.G.; validation, Z.T. and K.L.; formal analysis, Y.S.; investigation, Y.S. and Y.G.; resources, Z.T. and K.L.; writing—original draft preparation, Y.S.; writing—review and editing, K.L.; supervision, K.L.; project administration, K.L.; funding acquisition, K.L. All authors have read and agreed to the published version of the manuscript.

Funding: This research is funded by the National Natural Science Foundation of China (Grant Nos. 51475483).

Conflicts of Interest: The authors declare no conflict of interest.

References

1. Vassen, R.; Jarligo, M.O.; Steinke, T.; Mack, D.E.; Stöver, D. Overview on advanced thermal barrier coatings. *Surf. Coat. Technol.* **2010**, *205*, 938–942. [CrossRef]
2. Guo, H.B.; Gong, S.K.; Zhou, C.G.; Xu, H.B. Investigation on hot-fatigue behaviors of gradient thermal barrier coatings by EB-PVD. *Surf. Coat. Technol.* **2001**, *148*, 110–116. [CrossRef]
3. Guo, L.; Xin, H.; Zhang, Z.; Zhang, X.M.; Ye, F.X. Microstructure modification of Y_2O_3 stabilized ZrO_2 thermal barrier coatings by laser glazing and the effects on the hot corrosion resistance. *J. Adv. Ceram.* **2020**, *9*, 232–242. [CrossRef]
4. Guo, H.B.; Vassen, R.; Stover, D. Atmospheric plasma sprayed thick thermal barrier coatings with high segmentation crack density. *Surf. Coat. Technol.* **2004**, *186*, 353–363. [CrossRef]
5. Zhang, X.F.; Zhou, K.S.; Liu, M.; Deng, C.M.; Deng, C.G.; Song, J.B.; Tong, X. Enhanced properties of Al-modified EB-PVD 7YSZ thermal barrier coatings. *Ceram. Int.* **2016**, *42*, 13969–13975. [CrossRef]
6. Zhang, B.P.; Wei, L.L.; Gao, L.H.; Guo, H.B.; Xu, H.B. Microstructural characterization of PS-PVD ceramic thermal barrier coatings with quasi-columnar structures. *Surf. Coat. Technol.* **2017**, *311*, 199–205. [CrossRef]
7. Wang, Q.; Guo, L.; Yan, Z.; Ye, F. Phase composition, thermal conductivity, and toughness of TiO_2-doped, Er_2O_3-stabilized ZrO_2 for thermal barrier coating applications. *Coatings* **2018**, *8*, 253. [CrossRef]
8. Guo, L.; Li, M.Z.; Ye, F.X. Phase stability and thermal conductivity of RE_2O_3 (RE = La, Nd, Gd, Yb) and Yb_2O_3 co-doped Y_2O_3 stabilized ZrO_2 ceramics. *Ceram. Int.* **2016**, *42*, 7360–7365. [CrossRef]
9. Tsipas, S.A. Effect of dopants on the phase stability of zirconia-based plasma sprayed thermal barrier coatings. *J. Eur. Ceram. Soc.* **2010**, *30*, 61–72. [CrossRef]
10. Huang, H.; Liu, C.; Ni, L.Y.; Zhou, C.G. Evaluation of microstructural evolution of thermal barrier coatings exposed to Na_2SO_4 using impedance spectroscopy. *Corros. Sci.* **2011**, *53*, 1369–1374. [CrossRef]
11. Guo, L.; Zhang, C.L.; He, Q.; Li, Z.H.; Yu, J.X.; Liu, X.C.; Ye, F.X. Corrosion products evolution and hot corrosion mechanisms of $REPO_4$ (RE = Gd, Nd, La) in the presence of V_2O_5 + Na_2SO_4 molten salt. *J. Eur. Ceram. Soc.* **2019**, *39*, 1496–1506. [CrossRef]
12. Guo, L.; Li, M.Z.; He, S.X.; Zhang, C.L.; Wang, Q.; Ye, F.X. Preparation and hot corrosion behavior of plasma sprayed nanostructured $Gd_2Zr_2O_7$-$LaPO_4$ thermal barrier coatings. *J. Alloys Compd.* **2017**, *698*, 13–19. [CrossRef]
13. Li, S.; Liu, Z.G.; Ouyang, J.H. Growth of $YbVO_4$ crystals evolved from hot corrosion reactions of $Yb_2Zr_2O_7$ against V_2O_5 and Na_2SO_4 + V_2O_5. *Appl. Surf. Sci.* **2013**, *276*, 653–659. [CrossRef]
14. Zhou, X.; Xu, Z.H.; He, L.M.; Xu, J.Y.; Zou, B.L.; Cao, X.Q. Hot corrosion behavior of $LaTi_2Al_9O_{19}$ ceramic exposed to vanadium oxide at temperatures of 700–950 °C in air. *Corros. Sci.* **2016**, *104*, 310–318. [CrossRef]
15. Habibi, M.H.; Wang, L.; Liang, J.D.; Guo, S.M. An investigation on hot corrosion behavior of YSZ-Ta_2O_5 in Na_2SO_4 + V_2O_5 salt at 1100 °C. *Corros. Sci.* **2013**, *75*, 409–414. [CrossRef]
16. Liu, Z.G.; Ouyang, J.H.; Zhou, Y.; Zhu, R.X. Hot corrosion of V_2O_5-coated $NdMgAl_{11}O_{19}$ ceramic in air at 950 °C. *J. Eur. Ceram. Soc.* **2013**, *33*, 1975–1979. [CrossRef]
17. Loghman-Estarkia, M.R.; Razavia, R.S.; Edrisb, H.; Bakhshia, S.R.; Nejatic, M.; Jamali, H. Comparison of hot corrosion behavior of nanostructured ScYSZ and YSZ thermal barrier coatings. *Ceram. Int.* **2016**, *42*, 7432–7439. [CrossRef]
18. Habibi, M.H.; Wang, L.; Guo, S.M. Evolution of hot corrosion resistance of YSZ, $Gd_2Zr_2O_7$, and $Gd_2Zr_2O_7$ + YSZ composite thermal barrier coatings in Na_2SO_4 + V_2O_5 at 1050 °C. *J. Eur. Ceram. Soc.* **2012**, *32*, 1635–1642. [CrossRef]
19. Marple, B.R.; Voyer, J.; Thibodeau, M.; Nagy, D.R.; Vassen, R. Hot corrosion of lanthanum zirconate and partially stabilized zirconia thermal barrier coatings. *J. Eng. Gas Turbine Power* **2006**, *128*, 144–152. [CrossRef]
20. Zhong, X.H.; Wang, Y.M.; Xu, Z.H.; Zhang, Y.F.; Zhang, J.F.; Cao, X.Q. Hot-Corrosion behaviors of overlay-clad yttria-stabilized zirconia coatings in contact with vanadate-sulfate salts. *J. Eur. Ceram. Soc.* **2010**, *30*, 1401–1408. [CrossRef]
21. Jamali, H.; Mozafarinia, R.; Shoja-Razavi, R.; Ahmadi-Pidani, R. Comparison of hot corrosion behaviors of plasma-sprayed nanostructured and conventional YSZ thermal barrier coatings exposure to molten vanadium pentoxide and sodium sulfate. *J. Eur. Ceram. Soc.* **2014**, *34*, 485–492. [CrossRef]
22. Loghman-Estarki, M.R.; Razavi, R.S.; Jamali, H. Effect of molten V_2O_5 salt on the corrosion behavior of micro- and nano-structured thermal sprayed SYSZ and YSZ coatings. *Ceram. Int.* **2016**, *42*, 12825–12837. [CrossRef]

23. Loghman-Estarki, M.R.; Nejati, M.; Edris, H.; Razavi, R.S.; Jamali, H.; Pakseresht, A.H. Evaluation of hot corrosion behavior of plasma sprayed scandia and yttria co-stabilized nanostructured thermal barrier coatings in the presence of molten sulfate and vanadate salt. *J. Eur. Ceram. Soc.* **2015**, *35*, 693–702. [CrossRef]
24. Nejati, M.; Rahimipour, M.R.; Mobasherpour, I. Evaluation of hot corrosion behavior of CSZ, CSZ/micro Al_2O_3 and CSZ/nano Al_2O_3 plasma sprayed thermal barrier coatings. *Ceram. Int.* **2014**, *40*, 4579–4590. [CrossRef]
25. Liu, H.F.; Xiong, X.; Li, X.B.; Wang, Y.L. Hot corrosion behavior of Sc_2O_3-Y_2O_3-ZrO_2 thermal barrier coatings in presence of Na_2SO_4+V_2O_5 molten salt. *Corros. Sci.* **2014**, *85*, 87–93. [CrossRef]
26. Liu, Z.G.; Ouyang, J.H.; Zhou, Y.; Xia, X.L. Hot corrosion behavior of V_2O_5-coated $Gd_2Zr_2O_7$ ceramic in air at 700–850 °C. *J. Eur. Ceram. Soc.* **2009**, *29*, 2423–2427. [CrossRef]
27. Guo, L.; Li, M.Z.; Ye, F.X. Comparison of hot corrosion resistance of $Sm_2Zr_2O_7$ and $(Sm_{0.5}Sc_{0.5})_2Zr_2O_7$ ceramics in Na_2SO_4 + V_2O_5 molten salt. *Ceram. Int.* **2016**, *42*, 13849–13854. [CrossRef]
28. Chen, X.L.; Cao, X.Q.; Zou, B.L.; Gong, J.; Sun, C. High-Temperature corrosion behavior of plasma sprayed lanthanum magnesium hexaluminate coating by vanadium oxide. *J. Eur. Ceram. Soc.* **2015**, *35*, 227–236. [CrossRef]
29. Guo, L.; Li, M.Z.; Yang, C.X.; Zhang, C.L.; Xu, L.M.; Ye, F.X.; Dan, C.Y.; Ji, V. Calcium-magnesium-alumina-silicate (CMAS) resistance property of $BaLn_2Ti_3O_{10}$ (Ln = La, Nd) for thermal barrier coating applications. *Ceram. Int.* **2017**, *43*, 10521–10527. [CrossRef]
30. Guo, L.; Guo, H.B.; Ma, G.H.; Gong, S.K.; Xu, H.B. Phase stability, microstructural and thermo-physical properties of $BaLn_2Ti_3O_{10}$ (Ln = Nd and Sm) ceramics. *Ceram. Int.* **2013**, *39*, 6743–6749. [CrossRef]
31. Guo, H.B.; Zhang, H.J.; Ma, G.H.; Gong, S.K. Thermo-Physical and thermal cycling properties of plasma-sprayed $BaLa_2Ti_3O_{10}$ coating as potential thermal barrier materials. *Surf. Coat. Technol.* **2009**, *204*, 691–696. [CrossRef]
32. Chen, X.L.; Cao, X.Q.; Zou, B.L.; Gong, J.; Sun, C. Corrosion of lanthanum magnesium hexaaluminate as plasma-sprayed coating and as bulk material when exposed to molten V_2O_5-containing salt. *Corros. Sci.* **2015**, *91*, 185–194. [CrossRef]
33. Habibi, M.H.; Yang, S.Z.; Guo, S.M. Phase stability and hot corrosion behavior of ZrO_2-Ta_2O_5 compound in Na_2SO_4-V_2O_5 mixtures at elevated temperatures. *Ceram. Int.* **2014**, *40*, 4077–4083. [CrossRef]